Discontinuous Galerkin methods for turbulence simulation

By S. Scott Collis †

A discontinuous Galerkin (DG) method is formulated, implemented, and tested for simulation of compressible turbulent flows. The method is applied to turbulent channel flow at low Reynolds number, where it is found to successfully predict low-order statistics with fewer degrees of freedom than traditional numerical methods. This reduction is achieved by utilizing local *hp*-refinement such that the computational grid is refined simultaneously in all three spatial coordinates with decreasing distance from the wall. Another advantage of DG is that Dirichlet boundary conditions can be enforced weakly through integrals of the numerical fluxes. Both for a model advection-diffusion problem and for turbulent channel flow, weak enforcement of wall boundaries is found to improve results at low resolution. Such weak boundary conditions may play a pivotal role in wall modeling for large-eddy simulation.

1. Introduction

In this paper we formulate, implement, and apply a discontinuous Galerkin (DG) method for the simulation of compressible turbulent flows. Discontinuous Galerkin can be thought of as a hybrid of finite-volume and finite-element methods that has a number of potential advantages including: high-order accuracy on unstructured meshes, local *hp*-refinement, weak imposition of boundary conditions, local conservation, and orthogonal hierarchical bases that support multiscale turbulence modeling (Hughes *et al.* 2000; Collis 2001, 2002). The interested reader should consult the review of Cockburn (1999) and Cockburn *et al.* (2000) for a recent update on the status of discontinuous Galerkin. Since the DG method is ideally suited for hyperbolic or nearly hyperbolic systems, we believe that DG may be a particularly attractive method for high-Reynolds-number *compressible* turbulent flows in complex geometries. This paper takes a first step in applying DG to turbulent flows by considering low-Reynolds-number DNS of compressible turbulent channel flow. We note, before proceeding, that there is considerable ongoing research on DG methods (see Cockburn *et al.* 2000) and we have greatly benefited from the work of Cockburn and co-workers, Karniadakis and co-workers, and Bassi and Rebay.

2. Formulation

Consider the compressible Navier–Stokes equations in strong form

$$U_{,t} + F_{i,i} - F^v_{i,i} = S \quad \text{in } \Omega, \tag{2.1a}$$

$$U(x,0) = U_0(x) \quad \text{at } t = 0, \tag{2.1b}$$

where $U = \{\rho, \rho u, \rho e\}^T$ is the vector of conserved variables, ρ is the fluid density, u is the fluid velocity vector, and e is the total energy per unit mass. The inviscid and viscous
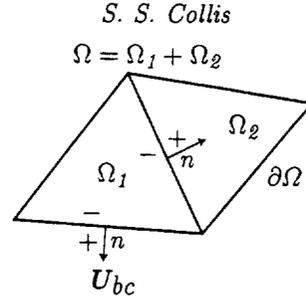
† Rice University, Houston, TX 77005, USA

FIGURE 1. Schematic of DGM discretization

flux vectors in the ith coordinate direction are $F_i(U)$ and $F_i^v(U)$, and S is a source term, including body forces in the momentum equations and a heat source in the energy equation. Equation (2.1a) is solved subject to appropriate boundary conditions, which must be specified for each problem of interest; a state equation, such as the ideal gas equation; and constitutive laws that define fluid properties such as viscosity and thermal conductivity as functions of the conserved variables. Due to space limitations, we do not explicitly define the flux vectors, state equation, or constitutive relations, but instead refer the reader to standard texts such as Hirsch (1988).

The fixed spatial domain for the problem is denoted by Ω, which is an open, connected, bounded subset of $I\!R^d$, $d = 2$ or 3, with boundary $\partial\Omega$. Let $\mathcal{P}_h$ be a partition of the domain Ω into N subdomains Ω_e where

$$\bar{\Omega} = \bigcup_{e=1}^{N} \bar{\Omega}_e \quad \text{and} \quad \Omega_e \cap \Omega_f = \emptyset \quad \text{for} \quad e \neq f. \tag{2.2}$$

Starting from the strong form of the compressible Navier–Stokes equations (2.1a), we consider a single subdomain, Ω_e, multiply by a weighting function W which is continuous in Ω_e, and integrate the flux terms by parts

$$\int_{\Omega_e} \left(W^T U_{,t} + W^T_{,i}(F_i^v - F_i) \right) dx + \int_{\partial\Omega_e} W^T \left(F_n - F_n^v \right) ds = \int_{\Omega_e} W^T S \, ds \tag{2.3}$$

where $F_n = F_i n_i$. If the solution were assumed to be continuous and this equation were summed over all the elements in $\mathcal{P}_h$, then all the flux terms would telescope to the boundary $\partial\Omega$ and we would obtain the standard continuous Galerkin form of the compressible Navier–Stokes equations. However, in discontinuous Galerkin, one instead allows the solution and weighting functions to be discontinuous across element interfaces (see figure 1) and the solutions on each element are coupled using appropriate numerical fluxes for both the inviscid flux $F_n(U) \to \widehat{F}_n(U^-, U^+)$ and the viscous flux, $F_i^v(U, U_{,j}) \to \widehat{F}_i^v(U^-, U_{,j}^-, U^+, U_{,j}^+)$. Introducing numerical fluxes and summing over all elements yields

$$\sum_{e=1}^{N} \int_{\Omega_e} \left(W^T U_{,t} + W^T_{,i}(F_i^v - F_i) \right) dx +$$
$$\sum_{e=1}^{N} \int_{\partial\Omega_e} W^T \left(\widehat{F}_n(U^-, U^+) - \widehat{F}_n^v(U^-, U_{,j}^-, U^+, U_{,j}^+) \right) ds = \sum_{e=1}^{N} \int_{\Omega_e} W^T S \, ds \tag{2.4}$$

where the U^+ and U^- states are defined in figure 1. For an element edge on the physical

boundary $\partial\Omega$, $U^+ = U_{bc}$. Likewise, for inter-element boundaries, U^+ comes from the neighboring element. Thus, all interface and boundary conditions are set through the numerical fluxes. Rewriting (2.4) in a more compact notation, the discontinuous Galerkin method is:

Given $U_0 = U_0(x)$, for $t \in (0, T)$, find $U(x, t) \in \mathcal{V}(\mathcal{P}_h) \times H^1(0, T)$ such that $U(x, 0) = U_0(x)$ and

$$B_{DG}(W, U) = (W, S) \qquad \forall W \in \mathcal{V}(\mathcal{P}_h), \tag{2.5}$$

where $\mathcal{V}(\mathcal{P}_h)$ is the broken space defined in Baumann & Oden (1999). If $\mathcal{V}(\mathcal{P}_h)$ is restricted to a space of continuous functions, then one recovers the classical continuous Galerkin approximation upon using the consistency properties of the numerical fluxes (Cockburn 1999).

While there is a wide range of choices for both the inviscid and viscous numerical fluxes (see Cockburn (1999) for a thorough review), we have initially chosen to use a Lax–Friedrichs method for the Euler flux

$$\widehat{F}_n(U^-, U^+) = \frac{1}{2}\left(F_n(U^-) + F_n(U^+)\right) + \lambda_m\left(U^- - U^+\right) \tag{2.6}$$

where λ_m is the maximum, in absolute value, of the eigenvalues of the Euler Jacobian $A_n = \partial F_n / \partial U$.

For the numerical viscous flux, we use the method of Bassi & Rebay (1997). First, a "jump savvy" gradient of the state, $\sigma_j \sim U_{,j}$ is computed by solving

$$\sum_{e=1}^{N} \int_{\Omega_e} V^T \sigma_j \, dx = -\sum_{e=1}^{N} \int_{\Omega_e} V_{,j}^T U \, dx + \sum_{e=1}^{N} \int_{\partial\Omega_e} V^T \widehat{U} n_j \, ds \qquad \forall V \in \mathcal{V}(\mathcal{P}_h) \tag{2.7}$$

for each direction, j, where

$$\widehat{U} = \frac{1}{2}\left(U^- + U^+\right) . \tag{2.8}$$

The Bassi–Rebay viscous flux is then computed using

$$\widehat{F}_n^v(U^-, \sigma_j^-, U^+, \sigma_j^+) = \frac{1}{2}\left(F_n^v(U^-, \sigma_j^-) + F_n^v(U^+, \sigma_j^+)\right) . \tag{2.9}$$

While this method is known to be only "weakly stable," (Arnold *et al.* 2002) we have not encountered any difficulties for the problems considered here, and this method has been used successfully in the past (Bassi & Rebay 1997). In the future, we will consider other, provenly-stable, numerical fluxes for the viscous terms, and the reader is referred to Arnold *et al.* (2002) for an extensive discussion of the advantages and disadvantages of a wide range of viscous fluxes for use in discontinuous Galerkin discretizations.

In setting boundary conditions weakly through the numerical fluxes, one must construct a state, U_{bc}, that enforces the appropriate boundary conditions, and Atkins (1997) provides a discussion of the important issues involved in selected U_{bc}. For the Navier–Stokes calculations reported here, we use the following approach. At far-field boundaries U_{bc} is set to freestream values. At isothermal wall boundaries, we evaluate U_{bc} separately for the convective and viscous fluxes. Let $q_1 = (u^- n_y - v^- n_x)n_y$ and

$q_2 = (v^- n_x - u^- n_y)n_x$ then the reconstructed state at a wall for the convective flux is

$$U_{bc} = \left\{ \begin{array}{c} \rho^- \\ \rho^- q_1 \\ \rho^- q_2 \\ \rho^- e^- + 0.5\rho^-(q_1^2 + q_2^2) \end{array} \right\}. \tag{2.10}$$

This state enforces the no-penetration condition which is appropriate for both inviscid and viscous calculations. For the viscous flux, the no-slip condition is enforced using

$$U_{bc} = \left\{ \begin{array}{c} \rho^- \\ 0 \\ 0 \\ \rho^- T_w/(\gamma(\gamma-1)M^2) \end{array} \right\} \tag{2.11}$$

where T_w is the prescribed wall temperature, γ is the ratio of specific heats, and M is the reference Mach number.

By way of summary, the discontinuous Galerkin method is a hybrid of finite-element and finite-volume methods, where solutions are continuous within an element but discontinuous across element interfaces, and elements are coupled via *numerical fluxes* on element interfaces. Discontinuous Galerkin has several potential advantages including: (1) Spectral accuracy on arbitrary meshes, (2) Local *hp*-refinement, (3) Boundary conditions are imposed weakly through numerical flux, (4) Local conservation allows for different fidelity models on neighboring elements, (5) Orthonormal hierarchical basis on each element readily supports multiscale turbulence models, and (6) DG works best near the hyperbolic limit making it potentially valuable for high Reynolds number turbulence. A thorough review of the DG method is available (Cockburn 1999) while a more complete description of DG for turbulence simulation including a discussion of multi-scale turbulence modeling is given in (Collis 2002).

3. Discretization and implementation

For every element $\Omega_e \in \mathcal{P}_h$ we define the finite-dimensional space $P_{p_e}(\hat{\Omega})$ of polynomials of degree $\leq p_e$ defined on a master element $\hat{\Omega}$. Then

$$P_{p_e}(\Omega_e) = \left\{ \phi | \phi = \hat{\phi} J_{\Omega_e}^{-1}, \hat{\phi} \in P_{p_e}(\hat{\Omega}) \right\} \tag{3.1}$$

where J_{Ω_e} is the Jacobian of the transformation of element Ω_e to the master element and

$$\mathcal{V}_p(\mathcal{P}_h) = \left(\prod_{e=1}^{N} P_{p_e}(\Omega_e) \right)^m \subset \mathcal{V}(\mathcal{P}_h) \tag{3.2}$$

where m is the number of conserved variables; $m = 5$ in three dimensions.

Thus, the semi-discrete discontinuous Galerkin method is: Given $U_0 = U_0(x)$, for $t \in (0, T)$, find $U_h(x, t) \in \mathcal{V}_p(\mathcal{P}_h) \times H^1(0, T)$ such that

$$B_{DG}(W_h, U_h) = (W_h, S), \qquad \forall W_h \in \mathcal{V}_p(\mathcal{P}_h). \tag{3.3}$$

We utilize the family of orthogonal, hierarchical bases formed from tensor products of Jacobi polynomials, as described in Karniadakis & Sherwin (1999), which are supported in a wide range of elements types in two and three dimensions. For time advancement, we currently use the third-order TVD-RK method (Shu 1988; Shu & Osher 1988)
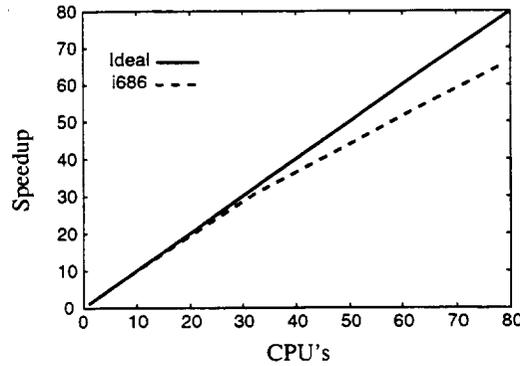
FIGURE 2. Typical parallel speedup for DG implementation on a Pentium IV Beowulf cluster.

The DG formulation presented above has been implemented using object-oriented programming (OOP) in fully modern ANSI/ISO C++ using the Standard Template Library and generic programming concepts. For efficiency, all kernel computations are performed using the ATLAS library, and the code runs on a number of operating systems including Linux, Windows, and SGI Irix. The code is implemented as an element library that supports all the operations required for discontinuous Galerkin, and we have used this library to implement specific solvers for advection-diffusion, Burgers, wave, linearized-Euler, Euler, Navier–Stokes equations. Due to the inherent locality in the discontinuous Galerkin discretization, parallel implementation is particularly easy and efficient. We use the MPI-2 library (including parallel MPI-IO) and parallel efficiency results are shown in figure 2 for our Pentium IV Beowulf cluster demonstrating excellent scaling.

4. Weak boundary conditions

One of the issues that arises in using discontinuous Galerkin methods is that Dirichlet boundary conditions are most naturally enforced weakly through the numerical fluxes. While similar "weak" boundary conditions have been used for far-field nonreflecting boundary conditions in finite-difference discretizations (see e.g. Poinsot & Lele (1992); Thompson (1987)) the use of weak boundary conditions for wall-type boundary conditions is less common, especially in the flow physics community. In the computational mechanics and applied mathematics communities there has been prior work on weak enforcement of Dirichlet boundary conditions in the continuous Galerkin method by Babuska (1973) and Nitsche (1971) and these methods are related to discontinuous Galerkin (Arnold *et al.* 2002). Likewise, the recent work of Layton (1999) provides theoretical considerations for weakly enforced Dirichlet boundary conditions for the Stokes problem that are motivated by observations of improved solution quality compared to hard Dirichlet boundary conditions.

While one can always set "hard" Dirichlet boundary conditions in any discretization (including DG), it is interesting to compare the performance of hard boundary conditions with weak enforcement through the numerical fluxes as described above. As an example, consider the simple steady forced advection-diffusion problem

$$u_{,x} = 1 + \nu u_{,xx} \tag{4.1}$$

with boundary conditions $u(0) = u(1) = 0$ and diffusivity $\nu = 0.01$. Figure 3 shows results computed using a discontinuous Galerkin discretization with two $p = 6$ elements and
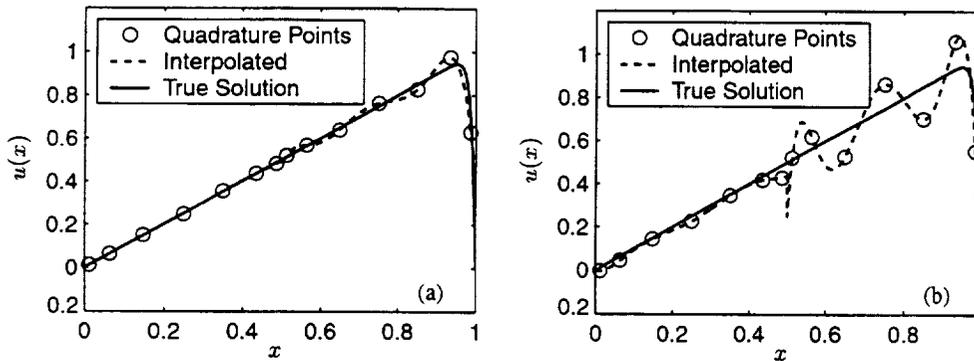
FIGURE 3. Weak (a) and hard (b) Dirichlet boundary conditions for an advection-diffusion problem

BC	L_∞	L_2	H_1
Weak	0.374	0.0198	2.00
Hard	0.251	0.0850	3.35

TABLE 1. Errors in advection diffusion solutions

both hard and weak enforcement of the Dirichlet boundary conditions. This discretization was intentionally selected to be coarse in order to highlight the differences between the two solutions. One clearly sees that oscillations are more pronounced when a hard boundary condition is used. Conversely, while oscillations are less in the weak case, the boundary condition on the right side (inside the boundary layer) is only approximately satisfied; $u(1) = 0.374$ instead of zero. Table 1 compares the error in the solution in the L_∞, L_2, and H_1 norms. Consistent with the graphical results, the solution with weak Dirichlet boundary conditions has four times less error in L_2 and is also better in H_1. However, the solution with weak boundary conditions is slightly worse in L_∞ and this is directly due to the error in the boundary value. Discarding a small region near $x = 1$, the weak solution is also better in L_∞. While these results are certainly not conclusive, they are indicative of the potential benefit to be gained from weak enforcement of Dirichlet boundary conditions that are naturally obtained from a DG discretization. Philosophically speaking, one should not enforce boundary conditions any more accurately then the error in the interior solution. Doing so tends to over-constrain the interior solution, typically leading to oscillations as seen in figure 3(b). By weakly enforcing boundary conditions one obtains solutions that still feel the influence of the boundary through the numerical fluxes, but in a manner that is consistent with the accuracy of the interior solution, leading to improved solutions away from the wall. Given the importance of wall boundary conditions for near-wall turbulence, we will pay particular attention to the success of the weak boundary condition throughout the following discussion.

5. Flow over a circular cylinder

Before applying our DG formulation to a turbulent flow, we begin by considering a benchmark problem of both steady and unsteady flow over a circular cylinder.

	DG $p = 4$		DG $p = 6$		FD 6th order		Experiment	
Re	s/d	C_d	s/d	C_d	s/d	C_d	s/d	C_d
20	0.96	2.125	0.96	2.124	0.93	1.98	0.9	2.01
40	2.39	1.589	2.39	1.589	2.36	1.50	2.1	1.48

TABLE 2. Drag and separation length for laminar flow over a circular cylinder, with comparison to prior computations and experiments. The computational and experimental data are taken from Visbal (1986).

5.1. Steady flow

Consider the steady, laminar flow of air past an isothermal circular cylinder kept at the freestream temperature. The freestream Mach number is $M = 0.2$ and results are reported for two Reynolds numbers: 20 and 40. By considering a series of different domain sizes, we eventually selected a domain of $\Omega = [-15, 30] \times [-30, 30]$ as sufficiently large to prevent adverse influence on the net drag and length of the separation bubble. A block structured mesh using 812 quadrilaterals was generated using a special purpose grid generator (Tezduyar 1991) and each quadrilateral has polynomial order of either $p = 4$ or $p = 6$. Table 2 compares the current DG results for the total drag coefficient, C_d, and separation bubble length, s/d, with prior high-order finite-difference computations and experiments. The DG results for both $p = 4$ and $p = 6$ are nearly identical, indicating that these quantities are converged. The DG results are within about 7% of the experimental results, which is a negligible difference given the difficulty of performing measurments at such low Reynolds numbers. Comparing the DG results to the prior finite-difference calculations of Visbal (1986) yields a difference of about 6% in C_d and less than 3% in s/d. Interestingly, Morgan et al. (2002) recently performed simulations using a block-parallel version of the same solver used by Visbal (1986) and they report up to 3% difference in both s/d and C_d. While the source of the discrepencies between these three codes is not known, the DG results are converged with regard to both domain size and resolution.

5.2. Vortex shedding

Next, consider unsteady vortex shedding from a circular cylinder. The Reynolds number based on diameter and freestream velocity is $Re = 100$, the freestream Mach number is $M_\infty = 0.2$ and an isothermal condition is enforced at the cylinder surface with $T_w = T_\infty$. We have performed simulations over a range of domain sizes and have investigated both h and p-refinement to establish the convergence properties of the method. For brevity, we show results only for a relatively large rectangular domain, of size $x_1 \in [-15, 30]$ and $x_2 \in [-30, 30]$, using 812 quadrilateral elements with a tensor-product basis of Legendre polynomials on each element, where the polynomial order varies from $p = 5$ to 8. We note in passing that this domain was found to be sufficiently large to prevent far-field boundary influence on the solution. Table 3 documents the convergence of the Strouhal number St, peak-to-peak lift coefficient ΔC_l, and average drag coefficient C_d with polynomial order. We see that even with $p = 4$ all quantities are accurate to three significant figures. When $p = 8$ the average drag coefficient is converged to at least 5 significant figures. The converged Strouhal number is $St = 0.1653$ which is in excellent agreement with the experimental value of 0.165 (Williamson 1989). For both the steady and unsteady cylinder flows, the weak implementation of wall boundary conditions is found to provide excellent results, even for rather coarse discretizations.

p	St	ΔC_l	C_d
4	0.1652	0.6951	1.4104
5	0.1652	0.6953	1.4105
6	0.1653	0.6958	1.4106
7	0.1653	0.6960	1.4107
8	0.1653	0.6960	1.4107
Exp†	0.165	–	–

TABLE 3. Convergence with polynomial order for vortex shedding from a circular cylinder at $Re = 100$.
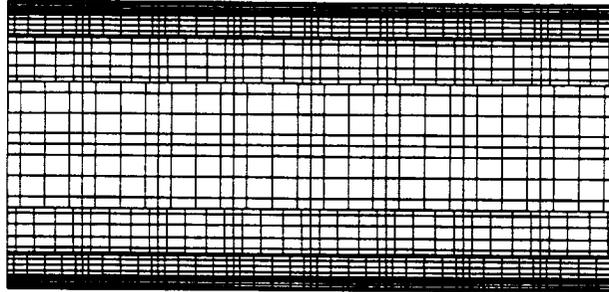†Experimental data is from Williamson (1989)

FIGURE 4. Cross-stream $(z$–$y)$ quadrature grid for the stretched mesh with $p = 5, 4, 3$.

6. Fully-developed channel flow

We now consider fully-developed turbulent flow in a plane channel with coordinates $x = x_1$ in the streamwise direction, $y = x_2$ in the wall-normal direction, and $z = x_3$ in the spanwise direction. The flow is assumed to be periodic in the streamwise and spanwise directions where the box size is selected so that the turbulence is adequately decorrelated in both directions. Coleman et al. (1995) provide excellent documentation of DNS results for compressible channel flows at low Re_τ.

As a first step towards utilizing DG for turbulent flows, we have performed DNS at $Re_\tau = 100$ with a centerline Mach number of $M_c = 0.3$ so that comparisons can be made directly to prior incompressible results (see e.g. Kim et al. (1987); Moser et al. (1999)). Following Coleman et al. (1995), we use a cold, isothermal wall so that internal energy created by molecular dissipation is removed from the domain via heat transfer across the walls, allowing a statistically steady state to be achieved. The bulk mass flow is held constant by the addition of an x_1-momentum source on the right-hand side of (2.1a).

The computational domain is $(4\pi, 2, 4\pi/3)$ and this is discretized with an array of $8 \times 8 \times 8$ elements yielding a total of 512 elements. Exploiting the flexibility of the DG discretization, we use both h and p refinement to more efficiently resolve flow features near the wall. In particular, two wall-normal distributions of elements are investigated. We first use a stretched mesh in the wall-normal direction where the grid points are given by

$$y_j = \frac{\tanh(c_s(2j/N_y - 1))}{\tanh c_s} + 1, \qquad j = 0, 1, \ldots, N_y \tag{6.1}$$

where $N_y = 8$. For this mesh, we reduce the polynomial order away from the wall, starting with two layers of $p = 5$ elements, then a layer of $p = 4$ followed by a layer of $p = 3$ elements near the centerline. Thus, moving from the bottom wall to the top
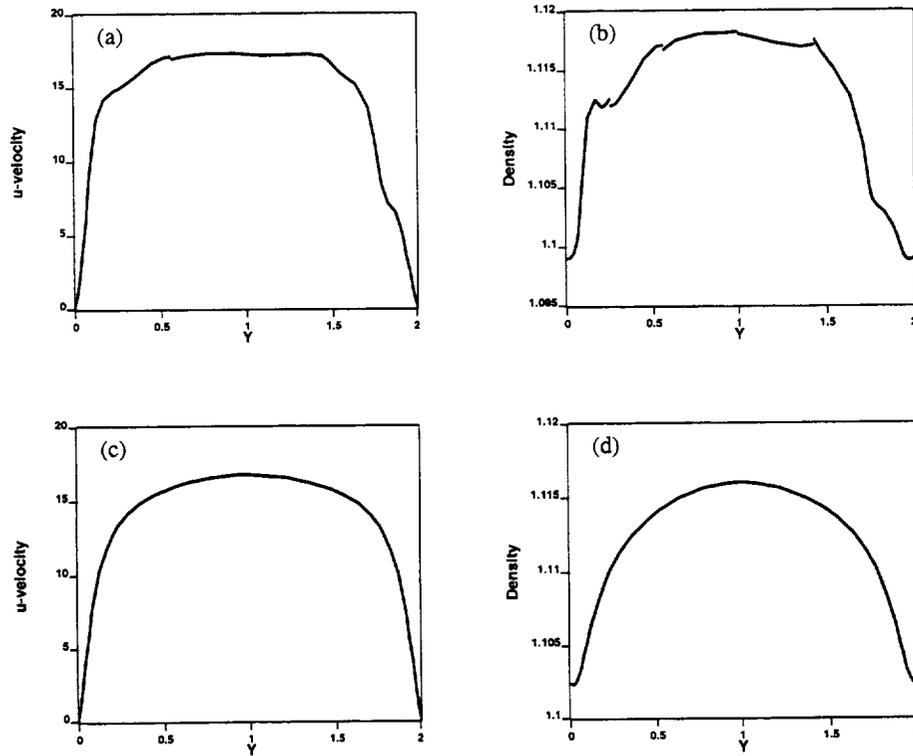
FIGURE 5. Discontinuities in instantaneous and averaged mean-flow profiles, $Re_\tau = 100$:
(a) instantaneous u, (b) instantaneous ρ, (c) average u, (d) average ρ.

wall, the element order varies like: $\{5, 5, 4, 3, 3, 4, 5, 5\}$ resulting in a total of 79,488 degrees of freedom. Note that the flexibility of the DG method makes it possible to coarsen simultaneously in *all three* coordinate directions as one moves away from the wall. The crossflow quadrature grid for the stretched mesh is shown in figure 4. We also have performed simulations using a uniform h mesh in the wall-normal direction but again with variable p order. For this mesh, two p distributions were considered: a low-resolution case with $p = \{5, 5, 4, 3, 3, 4, 5, 5\}$ yielding 79,488 degrees of freedom and a high-resolution case with $p = \{6, 6, 5, 4, 4, 5, 6, 6\}$ resulting in 131,456 degrees of freedom. In all cases, we use third-order TVD-RK time advancement with $\Delta t = 0.0001$. This time step is a factor of 10 smaller than that typically used in our incompressible code (Collis *et al.* 2000) because the incompressible code treats wall-normal viscous terms implicitly. We are currently enhancing our DG code to support implicit time-advancement.

We also note that computing turbulence statistics from a DG solution requires a substantial coding effort, so that currently we compute only mean and rms quantities. Higher-order statistics and spectra will be presented in the future.

We begin by plotting typical instantaneous and average u and ρ profiles for the stretched mesh solution in figure 5. In plotting all the results shown in this paper, no smoothing or other postprocessing has been done to remove the discontinuities inherent in a DG discretization. Thus, we can clearly see discontinuities in the instantaneous pro-
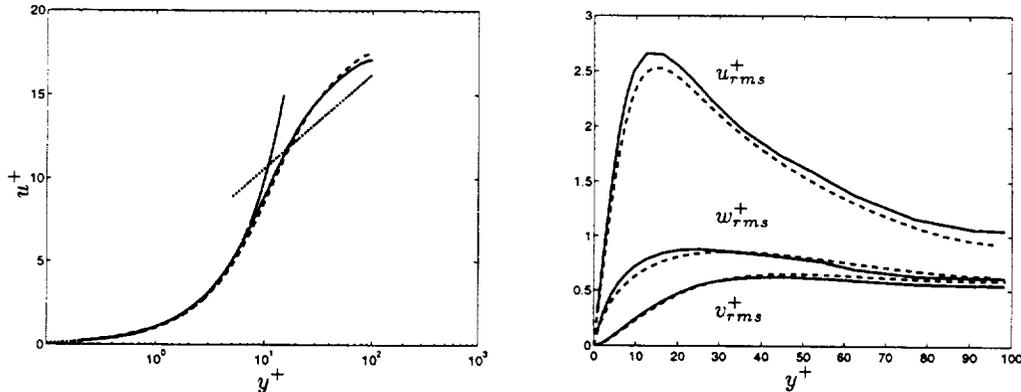
FIGURE 6. Mean and rms velocity profiles in wall units for the stretched mesh: ——— DG,
– – – – incompressible DNS, ········ law of the wall.

files, especially in ρ near the center of the channel. However, after averaging, both the streamwise velocity and density profiles are smooth. One of the nice features of DG is that if the solution is known to be smooth, then visible jumps in the solution are indicative of low resolution. Thus, with the stretched mesh, the instantaneous turbulent flow near the center of the channel is only marginally resolved, although near the walls even the instantaneous profiles appear smooth, indicating good resolution there. However, it is important to note that even though the resolution near the centerline may be marginal, the mean flow is well represented.

Evidence to support this claim is given in figure 6 which shows the mean and rms velocity profiles in wall units, compared to a reference incompressible DNS at the same Re_τ (Chang 2000). Both the mean and rms velocities are in excellent agreement with the incompressible DNS. Likewise, no discernible discontinuities are observed in either the mean or the rms profiles. We recall that the DG discretization uses 79,488 degrees of freedom and is formally between 4th- and 6th-order accurate, depending on the local polynomial order. For comparison, the incompressible DNS uses a hybrid Fourier-Galerkin method in the planes and second-order finite-volume method in the wall-normal direction and uses 336,960 degrees of freedom after dealiasing. Thus, the DG solution uses a factor of 4.2 less degrees of freedom (1.9 if dealiasing is not used in the incompressible case).

On the stretched mesh, the average slip in the streamwise velocity at the wall is 0.002% of the centerline velocity where the first collocation point is $\Delta y_w^+ = 0.7$ from the wall. †
To determine how the weak wall boundary condition influences the solution at coarser resolution (near the wall) we now consider results using a uniform mesh in the wall-normal direction. Figure 7 shows the mean streamwise velocity profiles in wall units as compared to the reference incompressible DNS, for both the low- and high-resolution cases. Interestingly, we see that the profiles are in excellent agreement with the reference solution. Such overlap clearly indicates that the mean shear stress is well predicted in both cases. However, careful examination of figure 7 does show that the law of the wall $u^+ = y^+$ is not perfectly satisfied at small y^+ because the flow slips at the wall. For the low resolution case, the slip velocity is 1% of the centerline velocity with $\Delta y_w^+ = 2$ while for the higher resolution case there is 0.68% slip with $\Delta y_w^+ = 1.6$. As expected, as near-wall resolution is increased, the amount of slip is reduced as the enforcement of the wall

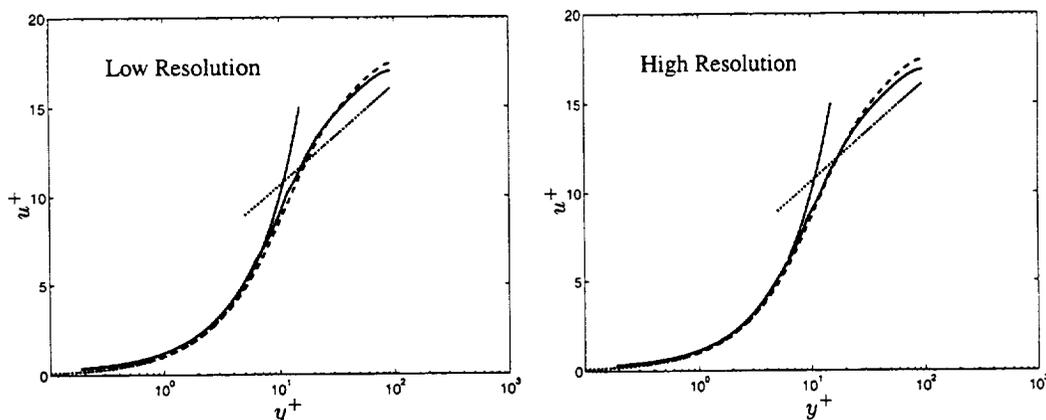† For reference, the centerline velocity is approximately $16u_\tau$ at $Re_\tau = 100$.

FIGURE 7. Effect of slip on mean velocity profile for the uniform mesh at two resolutions: ——— DG, — — — incompressible DNS, ········· law of the wall.
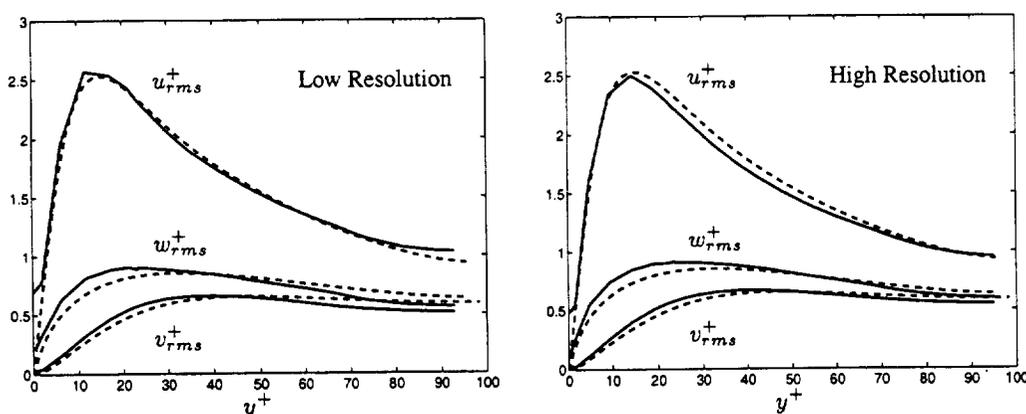

FIGURE 8. Effect of slip on rms velocity profiles for the uniform mesh at two resolutions: ——— DG, — — — incompressible DNS.

boundary condition improves (this is especially true for the stretched mesh). Importantly, the mean shear and the majority of the mean velocity profile are well predicted even for the lowest-resolution case when $\Delta y_w^+ = 2$, which is less than many RANS models allow.

Similar behavior is found for the rms velocities, as shown in figure 8 for the low- and high-resolution uniform-mesh cases. One can clearly see the slip in the streamwise rms velocities at the wall. For the low-resolution case $u_{rms}^+ = 0.65$ at the wall, while for the high-resolution case $u_{rms}^+ = 0.48$ at the wall. For reference, the stretched-mesh solution has $u_{rms}^+ = 0.0062$ at wall. Again, as resolution is increased in the near-wall region, the no-slip boundary condition is enforced to a higher accuracy. Importantly, with the exception of a region very close to the wall, both the mean and rms profiles throughout the channel are well predicted for all cases. Our prior experience with hard boundary conditions has shown that mean shear and rms profiles (i.e. turbulence production) are incorrectly predicted at low resolutions. Conversely, by enforcing the wall boundary conditions weakly through the numerical fluxes, the *influence* of the wall on the flow is correctly simulated in the form of net shear stress and turbulence production, even at resolutions for which the wall boundary values are inaccurate.

7. Conclusions

A discontinuous Galerkin method is formulated and implemented for simulation of complex, turbulent, compressible flows. The implementation is validated for both steady and unsteady separated flow over a circular cylinder, with results in excellent agreement with prior computations and/or experiments. An important feature of discontinuous Galerkin is the ability to enforce Dirichlet boundary conditions weakly, through numerical fluxes at the wall. The advantages of this approach are demonstrated for a simple advection-diffusion problem, where it it shown that enforcement of a weak boundary condition leads to a significant reduction in oscillations in the computed solution, resulting in a factor of 4 times less error in the L_2 norm. Applying DG to simulate fully-developed turbulent flow in a plane channel at low Reynolds number $Re_\tau = 100$ leads to results in excellent agreement with a reference incompressible DNS. The advantage of weak Dirichlet boundary enforcement is also demonstrated for this flow, where it is shown that accurate profiles of net shear stress, as well as mean and rms velocity, are obtained at low resolution—even resolution for which there is significant slip at the wall. In this context, weakly enforced wall boundary conditions may play a useful role in wall modeling for large-eddy simulation, where the wall-model is given by a particular numerical flux used at the wall.

REFERENCES

ARNOLD, D. N., BREZZI, F., COCKBURN, B. & MARIN, L. D. 2002 Unified analysis of discontinuous Galerkin methods for elliptic problems. *SIAM J. Numer. Anal.* **39**, 1749–1779.

ATKINS, H. L. 1997 Continued development of the discontinuous Galerkin method for compuational aeroacoustic applications. *AIAA Paper* 97-1581.

BABUSKA, I. 1973 The finite element method with penalty. *Math. Comp.* **27**, 221–228.

BASSI, F. & REBAY, S. 1997 A high-order accurate discontinuous finite element method for the numerical solution of the compressible Navier–Stokes equations. *J. Comp. Phys.* **131**, 267–279.

BAUMANN, C. E. & ODEN, J. T. 1999 A discontinuous hp finite element method for the Euler and Navier–Stokes equations. *Inter. J. Num. Meth. Fluids* **31**, 79–95.

CHANG, Y. 2000 Reduced order methods for optimal control of turbulence. *PhD thesis*, Rice University, Mech. Engg and Matls Sci.

COCKBURN, B., ed. 1999 *High-order methods for computational applications, Lecture Notes in Computational Science and Engineering*, chap. Discontinuous Galerkin methods for convection-dominated problems. Springer, Berlin.

COCKBURN, B., KARNIADAKIS, G. & SHU, C.-W., eds. 2000 *Discontinuous Galerkin Methods: Theory, Computation, and Applications*. Springer, Berlin.

COLEMAN, G. N., KIM, J. & MOSER, R. D. 1995 A numerical study of turbulent supersonic isothermal-wall channel flow. *J. Fluid Mech.* **305**, 159–83.

COLLIS, S. S. 2001 Monitoring unresolved scales in multiscale turbulence modeling. *Phys. Fluids* **13**, 1800–1806.

COLLIS, S. S. 2002 The DG/VMS method for unified turbulence simulation. *AIAA paper* 2002-3124.

COLLIS, S. S., CHANG, Y., KELLOGG, S. & PRABHU, R. D. 2000 Large eddy simulation and turbulence control. *AIAA Paper* 2000-2564.

HIRSCH, C. 1988 *Numerical Computation of Internal and External Flows, Vol. I: Fundamentals of Numerical Discretization.* Wiley, New York.

HUGHES, T. J. R., MAZZEI, L. & JANSEN, K. E. 2000 Large eddy simulation and the variational multiscale method. *Computing and Visualization in Science* **3**, 47–59.

KARNIADAKIS, G. E. & SHERWIN, S. J. 1999 *Spectral/hp Element Methods for CFD.* Oxford University Press.

KIM, J., MOIN, P. & MOSER, R. 1987 Turbulence statistics in fully developed channel flow at low Reynolds number. *J. Fluid Mech.* **177**, 133–166.

LAYTON, W. 1999 Weak imposition of the "no-slip" conditions in finite element methods. *Comp. Math. Appl.* **38**, 129–142.

MORGAN, P., VISBAL, M. R. & RIZZETTA, D. P. 2002 A parallel high-order flow solver for large-eddy and direct numerical simulation. *AIAA Paper* 2002-3123.

MOSER, R. D., KIM, J. & MANSOUR, N. N. 1999 Direct numerical simulation of turbulent channel flow up to $Re_\tau = 590$. *Phys. Fluids* **11**, 943.

NITSCHE, J. 1971 Über ein variationsprinzip zur lösung Dirichlet-problem bei verwendung von teilräumen, die kienen randbedingungen unteworfen sind. *Abh. Math. Sem. Univ. Hamburg* **36**, 9–15.

POINSOT, T. J. & LELE, S. K. 1992 Boundary conditions for direct simulations of compressible viscous flows. *J. Comp. Phys.* **101**, 104–128.

SHU, C.-W. 1988 TVD time discretizations. *SIAM J. Sci. Stat. Comp.* **9**, 1073–1084.

SHU, C.-W. & OSHER, S. 1988 Efficient implementation of essentially non–oscillating shock–capturing schemes. *J. Comp. Phys.* **77**, 439–471.

TEZDUYAR, T. E. 1991 Stabilized finite element formulations for incompressible flow computations. *Adv. Appl. Mech.* **28**, 1–44.

THOMPSON, K. W. 1987 Time-dependent boundary conditions for hyperbolic systems. *J. Comp. Phys.* **68**, 1–24.

VISBAL, M. 1986 Evaluation of an implicit Navier–Stokes solver for some unsteady separated flows. *AIAA Paper* 86-1053.

WILLIAMSON, C. 1989 Oblique and parallel modes of vortex shedding in the wake of a cylinder at low Reynolds numbers. *J. Fluid Mech.* **206**, 579–627.